

Geochemistry, Geophysics, Geosystems

Supporting Information for

Climactically driven changes in the supply of terrigenous sediment to the East China Sea

C. H. Anderson¹, R. W. Murray¹, A. G. Dunlea^{1,2}, L. Giosan³,

C. W. Kinsley⁴, D. McGee⁴, and R. Tada⁵

¹ Department of Earth and Environment, Boston University, Boston, MA, 02215, USA.

² Now at: Department of Geology & Geophysics, Woods Hole Oceanographic Institution, Woods Hole, MA 02543, USA.

³ Department of Geology & Geophysics, Woods Hole Oceanographic Institution, Woods Hole, MA 02543, USA.

⁴ Department of Earth, Atmospheric and Planetary Sciences, Massachusetts Institute of Technology, Cambridge, MA 02139, USA

⁵ Department of Earth and Planetary Science, University of Tokyo, Bunkyo-ku, Tokyo 113-0033, Japan

Contents of this file

Text S1 to S5

Figures S1 to S9

Additional Supporting Information (Files uploaded separately)

Dataset S1

S1. Age Model, Linear Sedimentation Rate, Dry Bulk Density, and Bulk Accumulation Rates

While the original drilling plans called for deep penetration and the anticipated recovery of Miocene-aged sediment, the sands of Unit B prevented recovery of materials deeper than 188 meters below seafloor (mbsf). Site U1429 was drilled after Site U1428 was abandoned, and the sands of Unit B were also recovered there as well.

The age models for both sites were based on shipboard micropaleontology, followed by shorebased analysis of benthic $\delta^{18}O$ and mapping to the global benthic stack using 28 tie points from the last 400 kyr (Sagawa et al., 2017). Linear sedimentation rates (LSR, cm/kyr) were determined from the age model itself. Dry bulk densities (DBD, g/cm³) were taken from shipboard measurements from Tada et al., (2013). Bulk accumulation rates (BAR, g/cm²/kyr) were calculated from the dry bulk density values and linear sedimentation rates for discrete samples. Here, we present the profiles of these parameters for completeness of comparison.

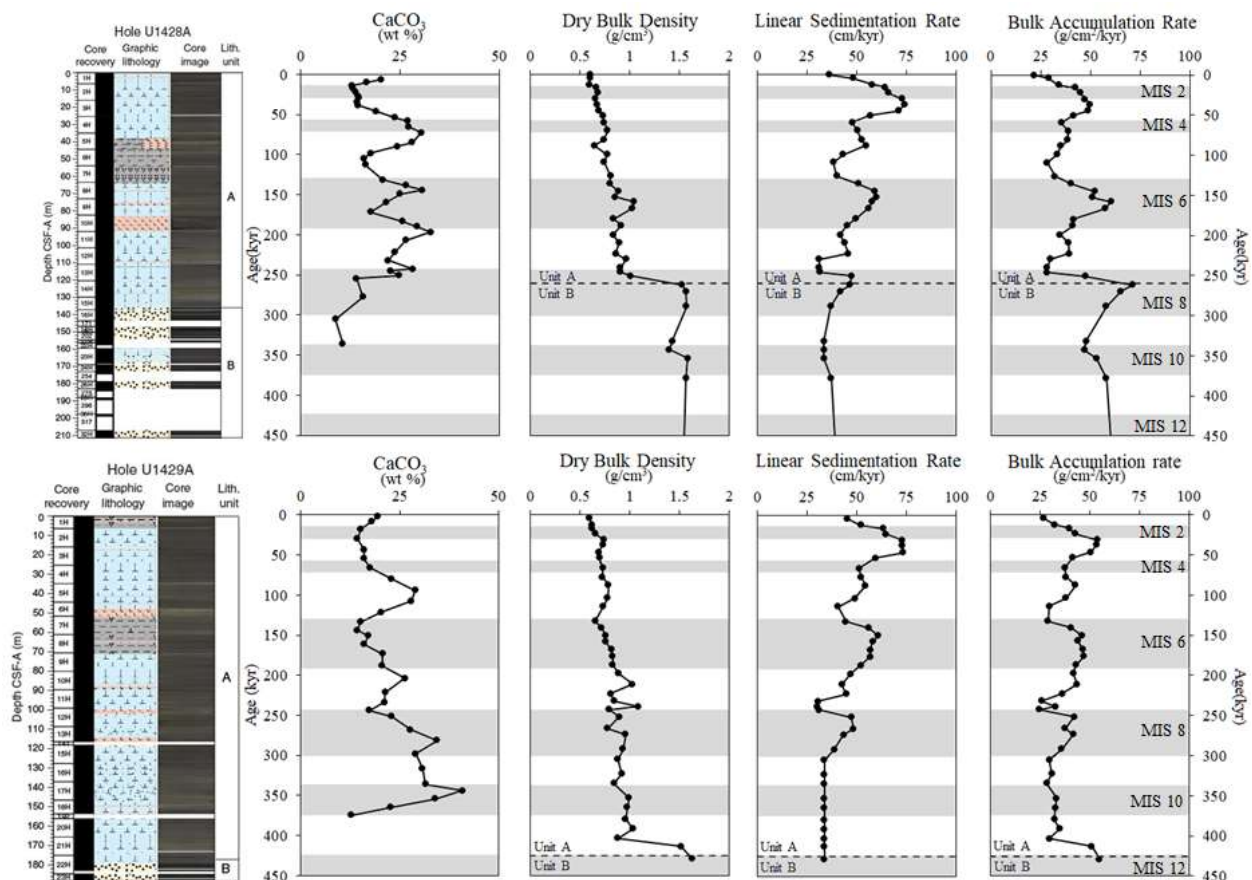


Figure S1. Shipboard lithologic summaries and CaCO₃ content (wt %) plotted vs. meters below seafloor (mbsf). Dry bulk density (DBD, g/cm³), linear sedimentation rate (LSR, cm/kyr), and bulk accumulation rates (BAR, g/cm²/kyr) with age (kyr) at IODP Sites

U1428 (top) and U1429 (bottom). LSR calculated from sample depth and age from the benthic age model (Sagawa et al., submitted September, 2017).

S2. Redox Chemistry

The geochemical characterization of Sites U1428 and U1429 is potentially complicated by the sub-oxic nature of the sediments and the potential for changes in oxygenation through time, which can influence mobilization and precipitation of certain elements. In this section, we use a suite of redox sensitive elements to investigate redox states. Although not the focus of this paper, this is important to ensure that that redox environment does not compromise the provenance signals and serves to further characterize the depositional environment of the Danjo Basin.

Interstitial water profiles at Site U1429 exhibit active Mn reduction in the upper 20 mbsf and sulfate reduction in the upper 50 mbsf of the sediment column (Expedition 346 Scientists, 2014), indicating reducing conditions at present. Selected redox sensitive elements in the sediment are often enriched above the elemental compositions of PAAS with few excursions less than this reference, as seen in Fe/Al (Fig. S4). Other element ratios (e.g., Cu/Al) express mixing between PAAS and CL reference values downhole, except for a pronounced decrease from approximately 210 to 240 kyr. Zn/Al and U/Al exhibit concentrations greater than PAAS and continental reference values, which may reflect in situ enrichment, as is common in reducing environments (Calvert and Pedersen, 1993; Morford and Emerson, 1999). The Zn-Cu-Mo ternary diagram (Fig. S5) indicates two compositionally different populations. These profiles collectively suggest periodic modestly reducing conditions.

To further investigate the reducing redox nature of the sites, an element suite consisting of Fe, Mn, V, Cu, Zn, Mo, and U was chosen to characterize the potential remobilization of these redox sensitive elements in the sediments. The redox QFA resulted in four significant factors that together explain 99% of the total variance in this dataset (Fig. S6). Factor 1 explains 32% of the variance and indicates that Fe, Mn, V, and Cu covary strongly. The covariance of Mn, Cu, and U in the second factor explains 32% of the variance. Factor 3 explains 32% of the variance and emphasizes Zn. The fourth factor explains ~2% of the variance and has high covariance of both Mn and U.

Considering these QFA groupings, the downhole profiles of these elements (Fig. S4) document relative depletions in Fe, Mn, and Cu at 70 to 80 kyr and 210 to 240 kyr, and relative enrichments in Zn and U, which collectively indicate reducing conditions (Calvert and Pedersen, 1993; Morford and Emerson, 1999). However, several elements (e.g., Mn, Zn, U) seem decoupled from each other in the QFA. The isolation of Zn and Mn into separate factors, and the combination of Mn and U into a separate factor, may indicate that these elements are currently associated with different phases. While additional research could target these redox variations in greater detail, given the moderate nature of the excursions in these profiles and that concentrations of key elements such as Mo are low (e.g., Mo < 5 ppm here, as opposed to many 10s of ppm in strongly reducing environments),

indicates that the redox environment is not compromising the putative provenance signal(s).

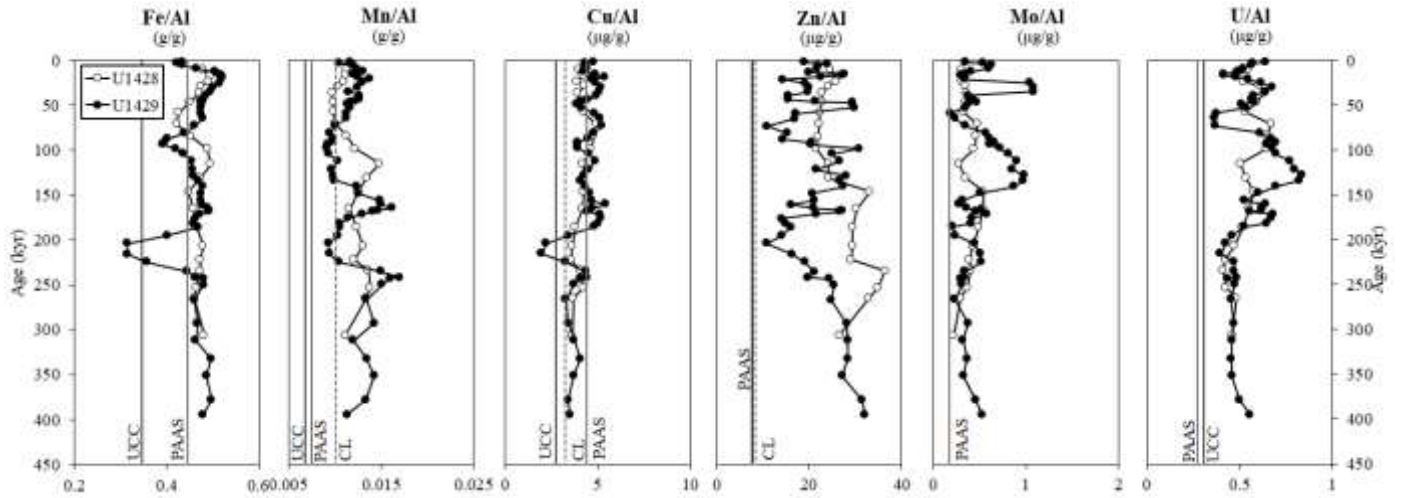


Figure S2. Redox-sensitive element ratio (g/g and μg/g) age profiles for both sites. Shown for reference, the gray vertical lines depict average values for upper continental crust (UCC), Chinese Loess (CL), post-Archean Australian average shale (PAAS) (Taylor & McLennan, 1985), and mid ocean ridge basalt (MORB) (Gale et al., 2013).

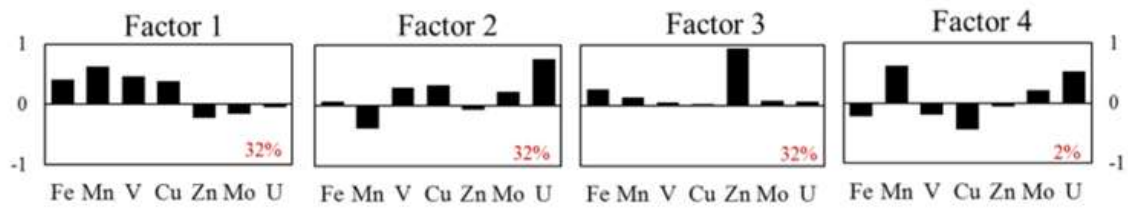


Figure S3. VARIMAX-rotated factor scores from QFA statistical analyses. Factors 1, 2, 3, and 4 from the QFA statistical analysis of redox sensitive elements. The variability of the data set explained by each factor is shown in each factor plot. The height of each bar indicates the VARIMAX-rotated factor scores of each element in each factor. The larger the bar (either up or down), the stronger the elements covary within each factor.

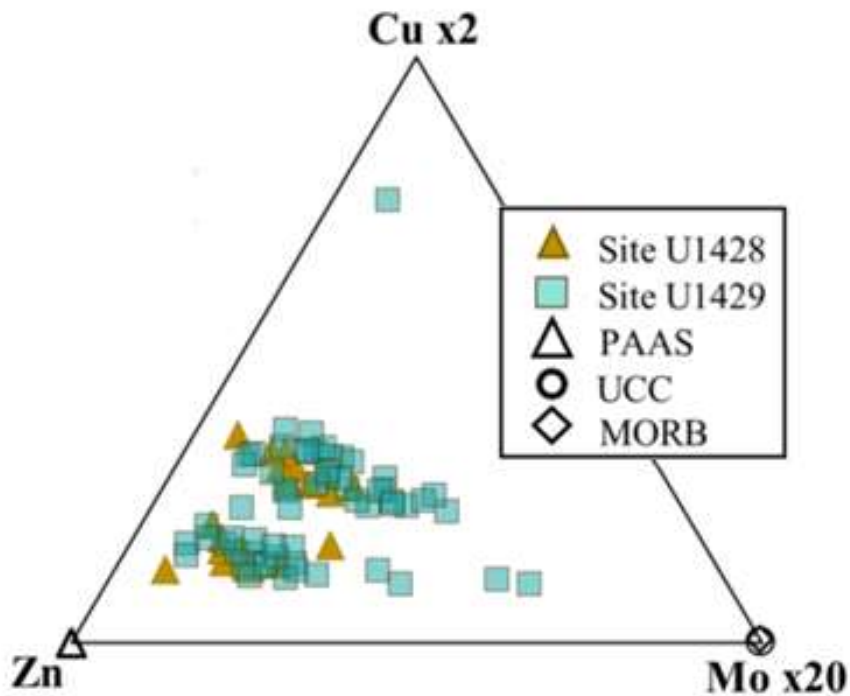


Figure S4. Bulk sediment samples plotted on ternary diagrams with end-member compositions. Zn-Cu-Mo separates two groups, and indicate mild reducing conditions.

S3. Geochemical Sample Preparation

All sample preparation and analysis were performed in the Analytical Geochemistry Facility at Boston University. Representative subsamples were freeze dried and hand powdered in an agate mortar and pestle for each discrete sample prior to digestion. Samples were dissolved via flux fusion as described most recently in Dunlea et al., (2015). Powdered sample was combined with lithium metaborate (LiBO₂) in an ultra-pure graphite crucible and heated at 1050°C for ten minutes to completely melt the sample and flux compound. Molten samples were then poured into 50 mL of 5% nitric acid and manually shaken (not stirred). The resulting solution was filtered through a 0.45µm Millex filter attached to a 12 mL HDPE plastic syringe, and re-diluted to 1:4000 by mass. These final solutions were analyzed via inductively coupled plasma emission spectrometry (ICP-ES; Jobin-Yvon Ultima-C) for all major (Si, Al, Ti, Fe, Mn, Ca, Mg, Na, K, P) and selected trace elements (Sc, V, Cu, Sr, Y, Ba).

Separate acid digestions were conducted for the analysis of additional trace elements and rare earth elements (REEs). Powdered sample was weighed into a Teflon™ vial with a cocktail consisting of double distilled concentrated hydrochloride, nitric, and hydrofluoric acids. Vials were sealed and heated at sub-boiling temperatures for 24 hours prior to sonication and neutralization by UltraPure grade H₂O₂ (Fisher, New Jersey, USA). Samples were then dried and re-dissolved in one mL of HNO₃ and one mL H₂O₂, and diluted 1:5000 by mass with 2% HNO₃. Final dilutions were analyzed by inductively coupled plasma mass spectrometry (ICP-MS, VG Plasma Quad ExCell).

Precision and accuracy are well-constrained. For each batch of samples, we analyzed three separate digestions of a homogenized, natural in-house sediment reference from Expedition 346, results of which indicated that the data are precise to within ~2% of the measured value for each element. To ensure accuracy, the international Standard Reference Material BHVO-2 was prepared and analyzed as an unknown in each analysis run on both instruments and compared to the accepted element concentrations. Measured BHVO-2 concentrations were consistently accurate within precision for the entire element suite (Ireland et al., 2014).

S4. Provenance Assessment: QFA, CLS, and Determination of Best-fit Models.

Our group uses extended Q-mode factor analysis (QFA) (e.g. Dunlea et al., 2015; Scudder et al., 2016; Ziegler et al., 2007 and references therein) to determine the minimum number of compositional factors to explain the maximum variability of the dataset. In QFA, each sample is treated as the result of mixing between specific factors, which are interpreted to represent the sediment sources. We use the MATLAB scripts published by Piasias et al., (2013) for this data exploration. To determine the minimum number of factors required to explain the dataset, additional QFA analyses are conducted by changing the number of factors used in the VARIMAX rotations. Factors are sequentially increased one by one, and then systematically decreased until the variance explained by the smallest factor is above our measurement error. This ensures that the identified number of factors is stable and sufficient to explain the most variance in the dataset. Care is taken to assess the sensitivity of the factor analysis techniques to identify the most robust factors to use in subsequent multiple linear regressions.

In this study, the QFA based on the refractory element menu resulted in five significant terrigenous factors that explain 99% of the variance of the dataset (Fig. 5). The first four factors are broadly similar, indicating that several aluminosilicates from different upper crustal sources of only slightly different compositions dominate the bulk sediment composition. Factor 1 is marked by strong covariance of Sc and La; Factor 2 has Al, Sc, and Cr covarying; in Factor 3 Al and Cr covary; and Factor 4 reflects covariance of Sc and Rb. These factors respectively describe 34%, 24%, 24% and 15% of the variance in the dataset. Although explaining only a small amount of the variance (3%), the 5th factor is required for complete modeling of the sequence. This Factor 5 emphasizes Ti, which we interpret as indicating either an enriched mafic end-member or an intermediate composition ash.

Once the minimum number of factors are identified via QFA, we then use iterative Constrained Least Squares (CLS) multiple linear regression techniques to test all possible combinations of potential compositional end-members. The CLS code described in Piasias et al. (2013) creates a multi-dimensional mixing model that determines the optimal proportions of each end-member by minimizing the sum of the square statistical residuals between the model and given sample dataset. As a final step, this CLS code generates the proportions of one set of specified end-members in each sample of the dataset. Previously, iterations of this code were laboriously repeated using different combinations of end-member compositions using geologically and geochemically reasonable potential end-members for the total number of factors identified via QFA. This process creates an abundance of outputs that can be unintentionally influenced by user selected end-members and neglect possible mixing outcomes.

To determine the best-fit CLS models, we use automatically generated iterative CLS multiple linear regression analyses based on the MATLAB scripts from Dunlea and Murray (2015). These CLS scripts are, at their core, identical to the codes in Piasias et al. (2013), but remove the labor intensive process of identifying the best fit end-members for CLS. However, it is necessary to return to the CLS codes of Piasias et al. (2013) to determine the final relative contributions of each end-member, or end-member families, to each sample for each iteration.

Using the geochemical database GEOROC (<http://georoc.mpch-mainz.gwdg.de/georoc/>), we geographically constrained possible end-members from the GEOROC collection of 15+ million global discrete data points. Data tabulated covers Asia, including the major deserts in China and Mongolia, Himalaya and Tibetan Plateau crust, well-characterized loess from the Chinese Loess Plateau, crust and volcanic material from Japan, as well as common generic reference material such as Upper Continental Crust (UCC) (Taylor and McLennan, 1985), Chinese Loess (CL) (Taylor et al., 1983), and Mid-Ocean Ridge Basalt (MORB) (Gale et al., 2013). Geochemical data was grouped by geographic region and type (e.g., continental crustal values of Chinese provinces, loess sequences, specific Japanese islands, and volcanic rocks of individual Japanese volcanoes), resulting in 160+ end-members to test. Extreme outliers were removed, remaining data was averaged for each discrete geographic area and rock type. A total of 110 potential end-members were used in the initial CLS models.

Following the initial CLS iteration, the potential end-member list was condensed for ease of calculation. Several additional CLS iterations were conducted to identify and remove or combine end-members that did not contribute to the top 1000 models. End-members of similar composition (e.g., loess values of similar geochemical composition), and/or geographic proximity (e.g., proximal Japanese islands to Kyushu, islands in the Ryuku Arc) were averaged within a locale where possible. The resulting end-member menu consisted of 23 potential end-members used in the final iterative CLS calculations (Table 1 in the main text).

In the final output of the iterative CLS code, we identified the best fit models by the models with the highest sum of coefficients. This parameter is the sum of all element coefficients of determination (that is, $r^2 \times 100$), to maximize the goodness of fit for each element within the CLS model. However, it is often not enough to only take the single “best” model, but to consider the top models collectively. For example, several end-member combinations commonly have negligible difference in goodness of fit, making patterns common to these collected models useful to select end-member combinations to consider further.

We identify the first set of end-member combinations with the sum of coefficients that are significantly higher than the next best end-member combination. When multiple end-member combinations create models that fit the data equally well and there is no a priori reason to prefer one model instead of the others, it is practical to average output fractions of each of the top best-fit model. In this dataset, we identified 11 models as the best fit from the top 300 models based on their sum of coefficients that were higher than the next best model (Fig. S1).

Care was taken to identify patterns in the end-member contributions in the top 11 best fit models. For example, UCC appears consistently as the first end-member; Luochuan and Xiashu Loesses appear as the second or third end-member and/ or paired with Chinese Loess; several Japanese islands and volcanic compositions appear as the fourth and fifth end-members (Figure S2).

Based on the patterns in the CLS output, end-member combinations that were equally well fit were combined to create compositional “families”, or categories of end-members. For example, specific Southern Island Chain and Ryukyu were combined into “Southern Japanese Islands” and Kyushu Volcanic composition was selected as the final end-member due to it encompassing the remaining Yufu-Tsurumi volcanic composition and its ubiquity in the fifth end-member. The resulting composite end-members were tested for model stability in iterative CLS tests as well as in the original CLS scripts. These end-members were then used in the final CLS iterations using the Piasias et al. (2013) MATLAB codes to calculate the relative contribution of each end-member in each sample.

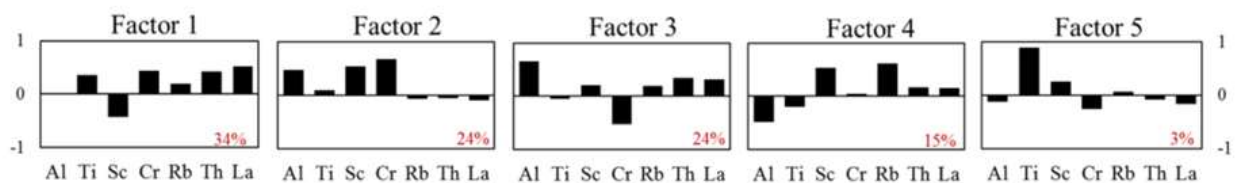


Figure S5. VARIMAX-rotated factor scores from QFA statistical analyses. Factors 1, 2, 3, 4, and 5 from the QFA statistical analysis of elements indicative of sediment provenance. The variability of the data set explained by each factor is shown in each factor plot. The height of each bar indicates the VARIMAX-rotated factor scores of each element in each factor. The larger the bar (either up or down), the stronger the elements covary within each factor.

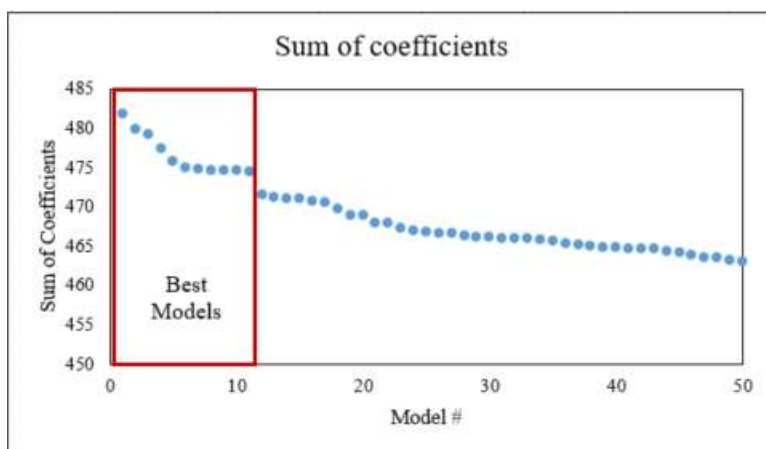


Figure S6. Sum of coefficients for the 50 best end-member combinations from iterative CLS calculation of 23 discrete end-members for 5 factors for Sites U1428 and U1429. Notice pronounced decrease in the sum of the coefficients between the 11th and 12th models, and therefore we considered the top 11 models to collectively be the most likely accurate explanation of the data.

Model #	End-members					Sum of Coefficients	
	EM1	EM2	EM3	EM4	EM5	sum_coef	sum_B
1	UCC	Average Luochuan	Southern Island Chain	Yufu-Tsurumi Average	Kyushu Volcanic	481.8462	5.6297
2	UCC	Avg Xiashu Loess	Southern Island Chain	Yufu-Tsurumi Average	Kyushu Volcanic	479.8649	5.6296
3	UCC	Average Luochuan	Avg Xiashu Loess	Southern Island Chain	Kyushu Volcanic	479.2031	5.6297
4	UCC	Average Luochuan	Kyushu Avg	Southern Island Chain	Kyushu Volcanic	477.4368	5.6297
5	UCC	A-MORB	Average Luochuan	Southern Island Chain	Kyushu Volcanic	475.8421	5.6298
6	UCC	Chinese Loess	Average Luochuan	Avg Xiashu Loess	Southern Island Chain	474.9328	5.6296
7	UCC	Chinese Loess	Average Luochuan	Southern Island Chain	Kyushu Volcanic	474.8296	5.6297
8	UCC	Avg Xiashu Loess	Kyushu Avg	Southern Island Chain	Kyushu Volcanic	474.7095	5.6296
9	UCC	Average Luochuan	Southern Island Chain	Shikoku	Kyushu Volcanic	474.642	5.6297
10	UCC	Average Luochuan	Southern Island Chain	Ryukyu Arc	Kyushu Volcanic	474.6017	5.6297
11	UCC	Average Luochuan	Kyushu and surrounding islands	Southern Island Chain	Kyushu Volcanic	474.5266	5.6297
12	UCC	Chinese Loess	Avg Xiashu Loess	Southern Island Chain	Kyushu Volcanic	471.4713	5.6296
13	UCC	Avg Xiashu Loess	Southern Island Chain	Shikoku	Kyushu Volcanic	471.2148	5.6296
14	UCC	Avg Xiashu Loess	Southern Island Chain	Ryukyu Arc	Kyushu Volcanic	471.0816	5.6296
15	UCC	Avg Xiashu Loess	Kyushu and surrounding islands	Southern Island Chain	Kyushu Volcanic	470.9763	5.6296
16	UCC	Average Luochuan	Avg Xiashu Loess	Kyushu and surrounding is	Southern Island Chain	470.72	5.6297
17	UCC	A-MORB	Average Luochuan	Kyushu and surrounding is	Southern Island Chain	470.4857	5.6297
18	UCC	Average Luochuan	Avg Xiashu Loess	Southern Island Chain	Shikoku	469.7825	5.6296
19	UCC	A-MORB	Average Luochuan	Southern Island Chain	Shikoku	468.9577	5.6297
20	Avg Shale (PAA)	UCC	Southern Island Chain	Yufu-Tsurumi Average	Kyushu Volcanic	468.8884	5.6299
21	UCC	Average Luochuan	Average Chinese Total Crust	Southern Island Chain	Kyushu Volcanic	467.9545	5.6298
22	Avg Shale (PAA)	UCC	Avg Xiashu Loess	Southern Island Chain	Kyushu Volcanic	467.9194	5.6299
23	UCC	Avg Xiashu Loess	Kyushu Avg	Kyushu and surrounding is	Southern Island Chain	467.2278	5.6296

Figure S7. Example output from CLS codes (Dunlea and Murray, 2015) for Sites U1428 and U1429 in this study. Patterns in end-member combinations make it possible to create compositional “families” to avoid selecting one compositionally similar end-member over another.

S5. Mass Accumulation Rates at Site U1428

In the main text of the paper we emphasize the data from Site U1429 since it extends further back in time. Here, we present the results from Site U1428 for completeness and comparison.

Site U1428 exhibits similar trends to Site U1429 in end-member contributions when the differences in sampling resolution are taken into account. We did several different exercises to examine the similarities and differences between the sites. We use the same five factors and resulting five end-members from the QFA and CLS modeling of both sites as a single dataset.

The generic Upper Continental Crust (UCC)-like end-member, possibly representing fluvially and/or eolian transported material from the Asian continent, is a robust component. At Site U1428, this UCC-like end-member contributes 48% to 67% of the total terrigenous fraction, with local maxima in contribution occurring between 24 to 47 kyr (67%), 70 to 84 kyr (67%) and 186 to 223 kyr (58%), as seen in Figure S8. The mass accumulation rate of the UCC-like end-member reaches a local maximum between 24 and 84 kyr, as MAR increases from a baseline of $10 \text{ g cm}^{-2} \text{ kyr}^{-1}$ up to $19 \text{ g cm}^{-2} \text{ kyr}^{-1}$ around 46 kyr (Figure S9). Following this local maxima, the UCC-like MAR decreases to $10 \text{ g cm}^{-2} \text{ kyr}^{-1}$ by approximately 130 kyr, before gradually increasing to $15 \text{ g cm}^{-2} \text{ kyr}^{-1}$ by the end of this record at approximately 240 kyr. The pattern of the UCC-like component at U1428 is comparable to the pattern at U1429. The contribution of the UCC-like component is generally greater through the record at Site U1429, and captures a similar peak in contribution and MAR between 18 to 47 kyr. However, the record at U1428 does not capture the variability in the UCC-like component seen in U1429 from 100 kyr and older, possibly due to the difference in sample density between these two sites.

The Chinese Loess end-members (Luochuan and Xiashu) exhibit less variability in contribution and MAR in the U1428 record compared to U1429. The Luochuan Loess end-member exhibits local maxima in contribution from 17 to 28 kyr (39%), and 130 to 146 kyr (48%) before decreasing down hole. A local minimum in contribution occurs from 84 to 98 kyr, reaching only 10% contribution in Site U1428. When present, the Xiashu Loess end-member reaches 8% contribution and is notable from 84 to 130 kyr (Figure S8). The presence of the Xiashu Loess component overlaps with the record at U1429, but finer details in both loess-like components are not captured in the lower resolution record at U1428. A gradual increase in Luochuan Loess MAR occurs between approximately 17 and 84 kyr, reaching a maximum accumulation rate of $10 \text{ g cm}^{-2} \text{ kyr}^{-1}$ (Figure S9). Xiashu Loess is consistently low in MAR, exhibiting its highest accumulation rate of $1.7 \text{ g cm}^{-2} \text{ kyr}^{-1}$ when present from 84 to 130 kyr. Both of these loess-like end-members exhibit accumulation rates that are approximately half the rates calculated at Site U1429 and may represent localized variability in sedimentation.

The Southern Japanese Islands (SJI) and Kyushu Volcanics end-members, likely representing fluvial material from the Japanese Archipelago and Japanese volcanic

material, respectively, contribute similar portions of the terrigenous fraction at both sites. At U1428, SJI ranges between 2% to 20% contribution, compared to 1% to 23% at Site U1429. Similarly, Kyushu Volcanics contributes 2% when present, similar to the 1 to 3 % at Site U1429. At the beginning of the record, SJI is at its maximum contribution (20%), and decreases to local minima of 4% at approximately 28 kyr and 2% at 115 kyr separated by a local maximum of 13% at 70 kyr. The contribution of SJI remains approximately 10% for the remainder of the record. The Kyushu Volcanics end-member is only present from 28 to 98 kyr and contributes 2% to the total terrigenous fraction. At Site U1428, SJI exhibits three localized peaks in accumulation rate, from the beginning of the record to 28 kyr ($3 \text{ g cm}^{-2} \text{ kyr}^{-1}$), 57 to 115 kyr ($3.2 \text{ g cm}^{-2} \text{ kyr}^{-1}$), and from 146 kyr to the end of the record ($2.5 \text{ g cm}^{-2} \text{ kyr}^{-1}$). The Kyushu Volcanics end-member reaches its maximum accumulation rate of $0.6 \text{ g cm}^{-2} \text{ kyr}^{-1}$ at 46 kyr, before decreasing to $0.18 \text{ g cm}^{-2} \text{ kyr}^{-1}$ for the remainder of the record, but despite these small accumulation rates this end-member is required to constrain the enrichment in Ti/Al towards more mafic compositions through time.

Overall, the ranges of end-member contribution and mass accumulation rates are similar between the two sites over the last 250 kyr. However, the lower sample resolution of Site U1428 obscures some of the finer features exhibited at Site U1429. The record at Site U1428 ends at approximately the time of the second peak in total accumulation rate at Site U1429, resulting in truncated and obscured direct comparisons.

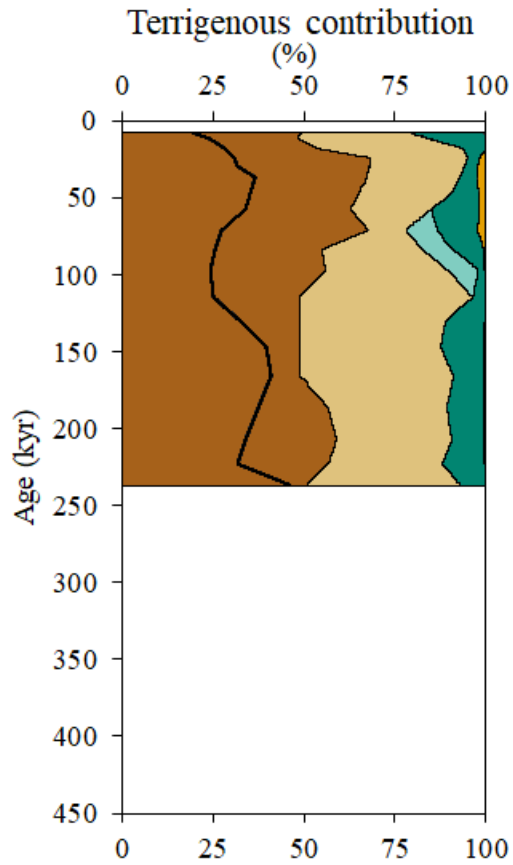


Figure S8. Terrigenous contribution of the five end-members produced by the provenance CLS multivariate models for site U1428. End-member contributions are plotted to sum to one-hundred percent, with each color representing the sum of each end-member contribution plus the end-members to the left.

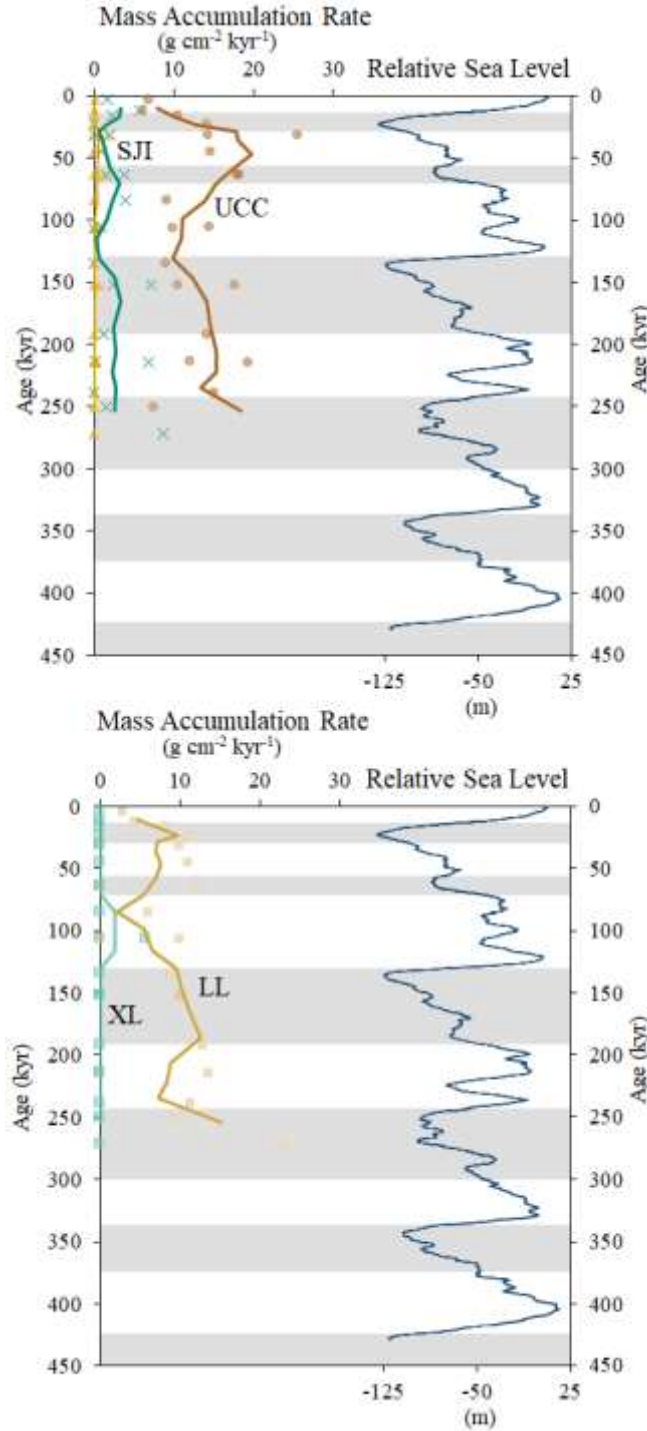


Figure S9. Mass accumulation rates (MAR) of the five end-members produced by the provenance CLS multivariate models for site U1428. Symbols represent individual sample values and solid lines indicate three-point moving averages of each end-member MAR. Relative Sea Level (m, blue line) and marine isotope stages are plotted for (Spratt and Lisiecki, 2016).

References

- Calvert, S.E., Pedersen, T.F., 1993. Geochemistry of Recent oxic and anoxic marine sediments: Implications for the geological record. *Mar. Geol.* 113, 67–88.
- Dunlea, A.G., Murray, R.W., 2015. Optimization of end-members used in multiple linear regression geochemical mixing models. *Geochemistry, Geophys. Geosystems* 16, 4021–4027. doi:10.1002/2015GC006132. Received
- Dunlea, A.G., Murray, R.W., Sauvage, J., Spivack, A.J., Harris, R.N., D'Hondt, S., 2015. Dust, volcanic ash, and the evolution of the South Pacific Gyre through the Cenozoic. *Paleoceanography* 30, 1–22. doi:10.1002/2015PA002829. Received
- Gale, A., Dalton, C.A., Langmuir, C.H., Su, Y., Schilling, J.G., 2013. The mean composition of ocean ridge basalts. *Geochemistry, Geophys. Geosystems* 14, 489–518. doi:10.1029/2012GC004334
- Ireland, T.J., Scudder, R.P., Dunlea, A.G., Anderson, C.H., Murray, R.W., 2014. Assessing the Accuracy and Precision of Inorganic Geochemical Data Produced through Flux Fusion and Acid Digestions: Multiple (60+) Comprehensive Analyses of BHVO-2 and the Development of Improved “Accepted” Values, in: AGU Fall Meeting. p. V41A–4767.
- Morford, J.L., Emerson, S., 1999. The geochemistry of redox sensitive trace metals in sediments. *Geochim. Cosmochim. Acta* 63, 1735–1750.
- Pisias, N.G., Murray, R.W., Scudder, R.P., 2013. Multivariate statistical analysis and partitioning of sedimentary geochemical data sets: General principles and specific MATLAB scripts. *Geochemistry, Geophys. Geosystems* 14, 4015–4020. doi:10.1002/ggge.20247
- Sagawa, T., Nagahashi, Y., Satoguchi, Y., Holbourn, A., Gallagher, S.J., Saavedra-Pellitero, M., Ikehara, K., Irino, T., Tada, R., 2017. Integrated tephrostratigraphy and isotope stratigraphy in the Japan Sea and East China Sea using IODP sites U1427, U1426 and U1429, Expedition 346 Asian Monsoon, *Prog. Earth Planet. Sci.* doi: 10.1186/s40645-018-0168-7
- Scudder, R.P., Murray, R.W., Schindlbeck, J.C., Kutterolf, S., Hauff, F., Underwood, M.B., Gwizd, S., Lauzon, R., McKinley, C.C., 2016. Geochemical approaches to the quantification of dispersed volcanic ash in marine sediment. *Prog. Earth Planet. Sci.* 3. doi:10.1186/s40645-015-0077-y
- Spratt, R.M., Lisiecki, L.E., 2016. A Late Pleistocene sea level stack. *Clim. Past* 12, 1079–1092. doi:10.5194/cp-12-1079-2016
- Tada, R., Murray, R.W., Alvarez Zarikian, C.A., 2013. Integrated Ocean Drilling Program Expedition 346 Scientific Prospectus Asian Monsoon Onset and evolution of millennial-scale variability of Asian monsoon and its possible relation with

Himalaya and Tibetan Plateau uplift. *Integr. Ocean Drill. Progr. Scientific Prospect.* 346. doi:10.2204/iodp.sp.346.2013

Taylor, S.R., McLennan, S.M., 1985. *The Continental Crust: Its Composition and Evolution.* Blackwell Scientific, Palo Alto.

Taylor, S.R., McLennan, S.M., McCulloch, M.T., 1983. Geochemistry of loess, continental crustal composition and crustal model ages. *Geochim. Cosmochim. Acta* 47, 1897–1905. doi:10.1016/0016-7037(83)90206-5

Ziegler, C.L., Murray, R.W., Hovan, S. a., Rea, D.K., 2007. Resolving eolian, volcanogenic, and authigenic components in pelagic sediment from the Pacific Ocean. *Earth Planet. Sci. Lett.* 254, 416–432. doi:10.1016/j.epsl.2006.11.049